CHEMISTRY OF MATERIALS

Open Access

This article is licensed under CC-BY 4.0

pubs.acs.org/cm

Article

Ion Migration and Dopant Effects in the Gamma-$CsPbI_3$ Perovskite Photovoltaic Material: Atomistic Insights through *Ab Initio* and Machine Learning Methods

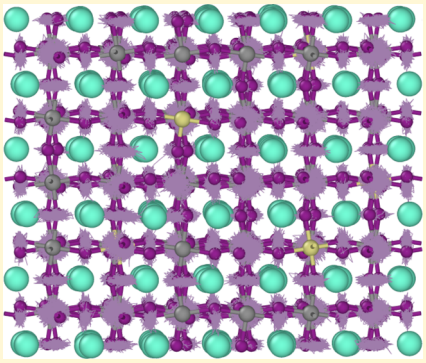
Allison Nicole Arber, Vikram, Felix C. Mocanu, and M. Saiful Islam*

Cite This: *Chem. Mater.* 2025, 37, 4416−4424

Read Online

ACCESS | Metrics & More | Article Recommendations | Supporting Information

ABSTRACT: Inorganic halide perovskites such as $CsPbI_3$ are attracting increasing attention for solar cell and optoelectronic applications. Ion migration is known to be an important factor in perovskite behavior, but the impact of cation dopants on iodide diffusion in the room-temperature orthorhombic γ-$CsPbI_3$ is not fully understood, especially at the atomic level. Here, we investigate the effect on iodide migration of incorporating different cations (including Sn^{2+}, Ba^{2+}, and Cu^{2+}) into γ-$CsPbI_3$, focusing on maintaining an inorganic phase rather than doping with molecular organic ions. Through a combination of *ab initio* and machine learning (ML) techniques, our results show that the simulated structure, band gap, and ion migration energies are in good agreement with experimental data. We find that partial Pb-site substitution does not have a major suppressing effect on iodide ion transport, which is important for guiding future doping work. An ML interatomic potential model was derived for large-scale simulations (∼80 ns) of the pristine and Sn-doped materials, which reveal iodide diffusion paths along the Pb−I octahedral edges with no correlated cation motion. Structural analysis indicates an ordered cation sublattice but disorder in the anion sublattice, indicative of high iodide ion mobility similar to fast-ion conductors.



1. INTRODUCTION

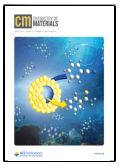
Halide perovskites are prime candidates for next-generation photovoltaic materials, largely due to their record-breaking power conversion efficiencies (PCE).[1,2] Currently, hybrid organic−inorganic perovskite PCEs have surpassed 26%,[3−5] while the inorganic perovskite $CsPbI_3$ has reached a record of 21.15%.[6,7] Perovskite solar cells, in contrast to silicon, benefit from easier and more cost-effective fabrication via either solution processing or vapor deposition.[8−11] The tunability of perovskite band gaps by elemental substitution also makes them excellent materials for use in single as well as multijunction solar cells.[12,13]

In particular, inorganic halide perovskites have higher thermal stability and are more resistant to degradation under light and high humidity than their hybrid counterparts.[14,15] This allows some $CsPbX_3$ (X = Cl, Br, I) compositions fabricated under atmospheric conditions to demonstrate 1−2 months of stability with minimal loss of efficiency[14,16] even without encapsulation.[14] This higher stability has sparked interest in γ-$CsPbI_3$ for single-junction cells. In addition, the band gap of 1.73 eV[17,18] is ideal for both silicon-perovskite and perovskite−perovskite tandem solar cells to push PCEs above the theoretical limits.[19,20] Inorganic lead halide perovskites have also gained interest for their applications in quantum dots and light-emitting devices due to their narrow emission and bright photoluminescence.[21−26]

Despite the increased stability of inorganic perovskites, these materials suffer from high intrinsic point defect concentrations (∼10^{14} cm^{-3})[27,28] which are dominated by halide vacancies. Halide vacancy-mediated diffusion has been shown to be the dominant mechanism for long-range ion transport in these perovskite systems.[29−32] This has been supported by the low activation energies (∼0.3 eV) for halide migration, as demonstrated by ionic conductivity studies[29−31] on similar inorganic perovskite halides (e.g., $CuPbI_3$ and $CsPbBr_3$). Intrinsic halide ion migration is known to be a leading cause of structural degradation[33] and voltage−current hysteresis,[33−37] both of which lead to a decrease in PCE over the cell's lifetime.

Recent studies[38−58] have found that certain cation dopants can modify structural stability and device performance, but there has not been any comprehensive study comparing the atomic-scale effects of cation dopants on ion migration barriers in $CsPbI_3$. The presence of dopants can introduce strain into the lattice, which can affect the iodide migration pathways and their activation energies. Inorganic dopants are of particular interest, as they can create such effects without introducing the

Received: February 28, 2025
Revised: May 29, 2025
Accepted: May 29, 2025
Published: June 10, 2025



© 2025 The Authors. Published by American Chemical Society

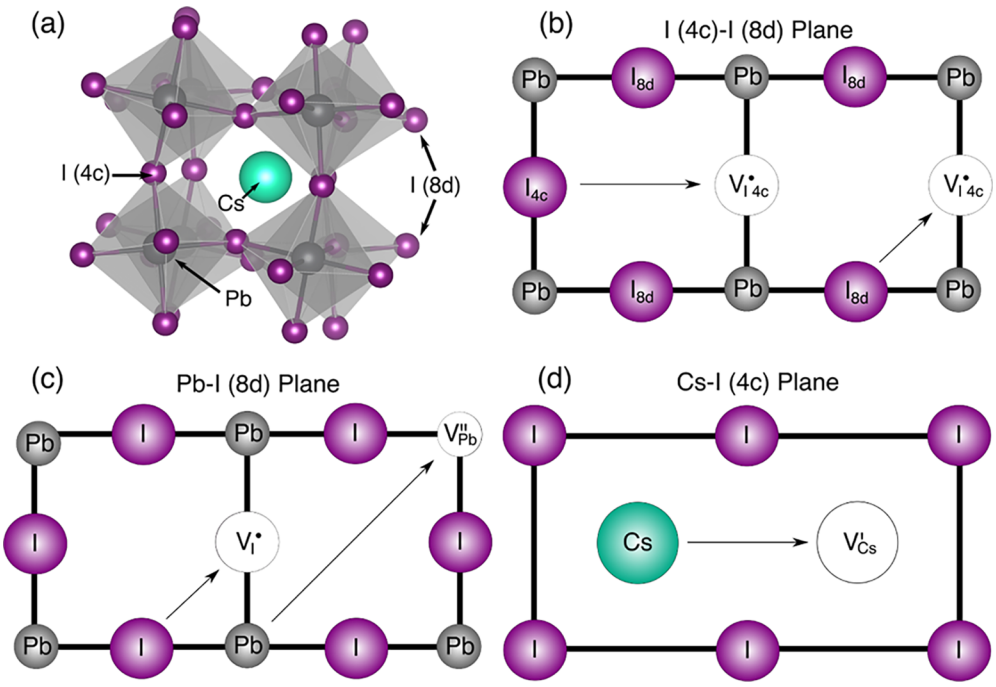


Figure 1. (a) Structure of γ-$CsPbI_3$ contains cesium cations, coordinated by 12 iodide ions, which are held within a lattice of PbI_6 octahedra. (b–d) The five migration pathways investigated in this work including I–I pathways between 8d and 4c sites.

volatility concerns associated with molecular organic cations.[13,14]

Previously related computational work on $CsPbI_3$[59,60] has largely focused on the cubic α-phase[61−64] which exists above 550 K,[65] with limited modeling studies on other phases.[41,66−69] However, structural studies[17,65,70] have demonstrated that, at room temperature, $CsPbI_3$ adopts the orthorhombic γ-polymorph perovskite structure (Figure 1a). The orthorhombic symmetry allows different possible migration pathways, as the iodide ions occupy two inequivalent Wyckoff positions with symmetries 4c and 8d. As such, there is a need for a comprehensive study that extends our understanding of ion migration to the γ-phase of the inorganic perovskite and explores the effects of dopants.

By focusing on the room-temperature orthorhombic phase (γ-$CsPbI_3$), this work investigates the various pathways of ion transport in the pristine material and explores the effects of a range of cation dopants using advanced atomistic modeling techniques. We first used *ab initio* density functional theory (DFT) calculations to model the structure of the pristine and doped γ-$CsPbI_3$ perovskite including the presence of iodide defects. Activation energy barriers associated with various iodide migration pathways were then obtained for a range of cation dopants, such as Sn^{2+}, Cu^{2+}, and Ba^{2+}. Although our focus is on isovalent 2+ cation substitution, certain aliovalent dopants (Ag^{+}, Bi^{3+}, Sb^{3+}) have been investigated experimentally[39,45,71] and are included in our modeling analysis for direct comparison.

To investigate ion diffusion over very long time scales (~80 ns) that are inaccessible using *ab initio*-based techniques, molecular dynamics (MD) simulations were performed for the first time on pristine and Sn-doped γ-$CsPbI_3$ using machine-learned interatomic potentials (MLIPs) trained with MACE,[72] a message-passing neural network (as detailed in the Methods section).

2. RESULTS AND DISCUSSION

2.1. Ion Transport in Pristine γ-$CsPbI_3$. Developing an accurate simulation model of the crystal structure and electronic band gap was the starting point of this study. Our model for γ-$CsPbI_3$ shows good agreement with experimental data, reproducing the structural lattice parameters[17] to within 2% and the band gap to within 0.13 eV of the measured value from photoluminescence studies[13] (Table 1). We then

Table 1. Comparison of Experimental[13,17] and Calculated Structural Properties (Lattice Constants, Angles, and Bond Distances) and Band Gap of γ-$CsPbI_3$

Parameter	Experiment	Calculated	Difference
a/Å	8.86	8.71	−0.15
b/Å	8.58	8.68	0.10
c/Å	12.47	12.44	−0.03
Mean angle/°	90.00	90.00	0.00
Cs–I bond/Å	4.42	4.43	0.01
Pb–I bond/Å	3.18	3.18	0.00
Band gap/eV	1.72	1.60	0.12

investigated the formation energetics of the full Schottky and iodide Frenkel defects. The Schottky defect consists of a formula unit of vacancies, and the Frenkel defect is formed by a vacancy and interstitial pair (eqs. S1, S2). We found the $CsPbI_3$ Schottky defect to have the lowest energy (0.18 eV/defect) and hence to be more stable compared to the iodide Frenkel (0.58 eV/defect), in good agreement with previous work on perovskite iodides.[73] These values support the current understanding that Schottky-type defects lead to the high intrinsic defect densities in these perovskites, causing the vacancy-mediated diffusion of iodide ions.[29−32] It is worth noting that long-range iodide interstitial diffusion in inorganic perovskite halides (or oxides) has not been observed experimentally due to the lack of interstitial space for large

https://doi.org/10.1021/acs.chemmater.5c00503
Chem. Mater. 2025, 37, 4416−4424

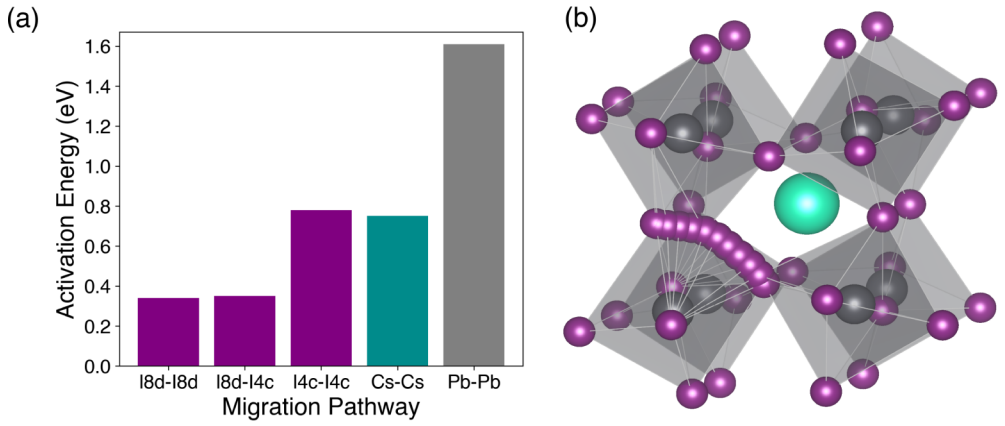


Figure 2. (a) Activation energy barriers for all the possible migration pathways (illustrated in Figure 1) in γ-$CsPbI_3$; (b) the I8d-I8d migration pathway; the most favorable pathways correspond to I migration between 8d-8d or 8d-4c sites, following a slightly curved path.

anions in such close-packed structures. Indeed, iodide vacancies as the primary mobile point defects were confirmed by measurements of the ionic conductivity as a function of iodine partial pressure.[32]

As noted, the symmetry of the room-temperature stable orthorhombic γ-$CsPbI_3$ lattice allows for different possible migration pathways, which have not been previously studied. Figure 1 illustrates the various Wyckoff symmetry sites in the γ-$CsPbI_3$ lattice (Figure 1a) and the ion migration pathways investigated in this work, which involve conventional hopping between neighboring lattice sites (Figure 1b–d).[33] The pathways investigated were (i) I migration between neighboring sites in the Cs–I plane (4c site); (ii) I migration along an octahedron edge between the Pb–I plane (8d site) and the Cs–I plane (4c site); (iii) I migration along an octahedron edge in the Pb–I plane (8d site); (iv) Pb migration along the diagonal <220> direction; and (v) Cs migration into a neighboring A-site vacancy within the Cs–I plane (4c site). The plane comprised of Pb and I 8d atoms (Figure 1c) is parallel to the Cs–I plane (Figure 1d) and contains the migration pathways of both Pb and I 8d ions to their respective vacancy sites. The plane containing both symmetry iodide sites (Figure 1b) is orthogonal to the other two planes and shows the migration of I 4c ions as well as transport between the two iodide sites. Energy barriers can be derived for these mechanisms by performing a series of transition-state calculations between adjacent sites. The calculated activation energies for these migration pathways are listed in Figure 2.

We found that iodide ion migration along the PbI_6 octahedral edge has the lowest activation energies of 0.34 and 0.35 eV between 8d-8d and 8d-4c sites, respectively. Energy profiles for the I migrations are shown in Figure S1. The comparatively high activation barriers for Cs and Pb indicate that these migrations are less likely, suggesting an immobile cation sublattice. We also found that the long I 4c-4c migration path has a high activation energy, which strengthens our understanding that I migration occurs only along the PbI_6 octahedral edges. These energies correlate well with values from previous experimental and computational studies of inorganic halide perovskites summarized in Table 2 with most values falling in the range of 0.3–0.4 eV for Pb-based perovskites. These results confirm that halide ions are the dominant migrating species in these perovskites, with relatively low migration barriers. Interestingly, analysis of the migration paths in γ-$CsPbI_3$ reveals a small deviation from the linear route, involving a curved path between iodine sites with the saddle point slightly bowed away from the adjacent Pb ion (shown in Figure 2). This atomic-scale feature is difficult to observe using experimental techniques alone. Such curved migration paths have been found previously in modeling studies of $MAPbI_3$[33] and the $LaGaO_3$ perovskite oxide-ion conductor,[74] which were subsequently confirmed by experimental neutron diffraction maximum entropy methods.[75]

Table 2. Summary of Experimental and Calculated Activation Energies for Halide Ion Migration in a Range of Inorganic Halide Perovskites from Previous Studies and This Work

Compound	Activation Energy (eV)	Technique/Reference
$CsPbCl_3$	0.29	Expt: ionic conductivity[29]
$CsPbBr_3$	0.25	Expt: ionic conductivity[29]
$KMnCl_3$	0.39	Expt: ionic conductivity[29]
$CuCdCl_3$	0.36	Expt: ionic conductivity[76]
$CsPbCl_3$	0.17	Expt: ionic conductivity[30]
$CsPbBr_3$	0.17	Expt: ionic conductivity[30]
$KMnCl_3$	0.65	Expt: ionic conductivity[77]
$CsCdCl_3$	0.73	Expt: ionic conductivity[77]
$CsSnBr_3$	0.23	Expt: ionic conductivity[77]
$CuPbI_3$	0.29	Expt: ionic conductivity[31]
$CsPbI_3$	0.38	Expt: selective blocking[78]
α-$CsPbI_3$	0.36	Calc: DFT[37]
α-$CsPbBr_3$	0.44	Calc: MD[79]
α-$CsPbBr_2I$	0.33	Calc: MD[79]
α-$CsPbBrI_2$	0.49	Calc: MD[79]
α-$CsPbI_3$	0.53	Calc: MD[79]
γ-$CsPbI_3$	0.34	Calc: DFT-NEB (this work)
γ-$CsPbI_3$	0.42	Calc: MLIP (this work)

2.2. Effect of Dopants on Ion Migration Barriers.

Benchmarking the migration pathways in the pristine structure allowed us to explore the effect of various dopants on the iodide migration pathways and the activation barriers. Previous experimental studies[38−58] propose a variety of inorganic dopants to improve photovoltaic (PV) performance, but the precise effects on ion migration have not been fully characterized. Here, we extend our related modeling work on ion migration in pristine and doped $MAPbI_3$ and $FAPbI_3$ perovskites[33,38,80−82] to provide a comprehensive comparison of the effect of cation dopants on I migration energies in γ-$CsPbI_3$. A range of B-site dopants were investigated, including

https://doi.org/10.1021/acs.chemmater.5c00503
Chem. Mater. 2025, 37, 4416−4424

Ba^{2+}, Cu^{2+}, Zn^{2+}, Ge^{2+}, Cd^{2+}, and Sn^{2+} at a typical low 3% concentration to retain the same 3D perovskite structure and because phase segregation can occur at high dopant substitution levels. The pathway studied in each case was the I vacancy migration between adjacent 8d symmetry sites, which we found has the lowest activation energy for migration and allowed us to probe trends in ion migration energies in a systematic manner. These B-site dopants were placed at the center of the octahedron within which the migration occurs.

The resulting ion migration activation barriers (Figure 3) indicate three main features. First, none of the wide range of

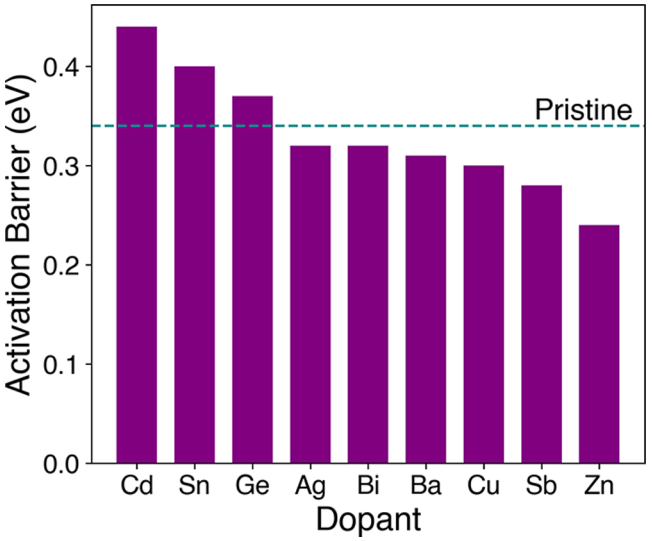


Figure 3. Activation energies for I vacancy migration in γ-$CsPbI_3$ between neighboring 8d sites near a dopant atom at the Pb site.

cation dopants led to an appreciable increase in activation energy, and in fact, several dopants decreased the activation energy. Hence, the results suggest that dopants such as Zn would not significantly suppress iodide ion migration in γ-$CsPbI_3$, which is important in guiding future doping studies. Second, structural analysis at the atomistic level found that dopants with a high barrier such as Cd or Sn have rigid structures during ion migration, whereas dopants like Zn cause local structural relaxations, resulting in lower energy iodide ion migration. Interestingly, the dopant-iodide bond distances at the transition state around the Zn dopant are reduced by ~0.3 Å in comparison to those of Cd and Sn. Other structural properties were also analyzed, including the dopant ion radius and the dopant-iodide bond length at the migration transition state. There do not appear to be any overarching design rules that predict the trends in activation barriers for these dopants, although the magnitude of the energy differences is relatively small. A key feature that differentiates the highest-barrier pathways from the lowest barrier pathways is the lack of any structural rearrangement before or after iodide ion migration. Third, the dopants Cd and Sn cause small increases in the activation energy when doped on the Pb site. While Cd results in a higher activation energy, its high toxicity[83] makes it an undesirable dopant. In contrast, Sn is a promising candidate due to the increasing interest of the scientific community in mixed Pb−Sn perovskites.[84] Mixing Sn in suitable quantities (~50−60%) at the Pb site improves carrier mobility and allows stronger optical absorption by reducing the band gap. The band gap tunability allows mixed Pb−Sn perovskites to be used in stand-alone or tandem solar cell applications. Although beyond the scope of the current investigation, it is worth noting that there has been recent interest in the role of oxidized tin (Sn^{4+}) in suppressing ion migration[82] as well as the use of molecular additives or defect passivation to improve the efficiency and stability of $CsPbI_3$ solar cells.[6,15,85]

2.3. Machine Learning Model of Ion Diffusion in γ-$CsPbI_3$. An important factor for understanding the transport flux through the perovskite absorber layer is the rate of iodide ion diffusion. To complement the migration barrier simulations and to gain insights into long-range diffusion rates, we employed a machine learning (ML) architecture of message-passing atomic cluster expansion (MACE)[72] to derive a single ML interatomic potential (MLIP) model (detailed in Methods). The model was used to run MD simulations of pristine and 3% Sn-doped γ-$CsPbI_3$. As noted, we focus here on the Sn dopant due to the growing interest in mixed Pb−Sn perovskites for band gap tunability and for potential application in tandem solar cells.

Using the trained MLIP, long-time-scale MD simulations were performed on pristine and Sn-doped γ-$CsPbI_3$ compositions, which have not been widely applied to examine ion diffusion in inorganic perovskite halides. Each of these compositions included representative concentrations of iodide vacancies, in line with the DFT calculations (Figure S2). While maintaining quantum mechanical accuracy at reduced computational cost, the MD simulations were run for a temperature range of 300−500 K and for a long time scale of ~80 ns, which is orders of magnitude greater than current *ab initio* MD. Diffusion coefficients (D_I) for the mobile iodide ions were derived from the temperature-dependent mean square displacements (MSDs) (Figure S3) and the activation barriers were calculated via the Arrhenius relationship, as displayed in Figure 4. MSD analysis demonstrates that ~80 ns is sufficient to achieve the conversion (Figure S4).

The resulting activation barriers of 0.42 and 0.43 eV for the pristine and Sn-doped systems, respectively, are in good agreement with experimental values (Table 2) and with our DFT results. We note that, despite the small difference in activation energies from MD vs DFT-NEB, these values are

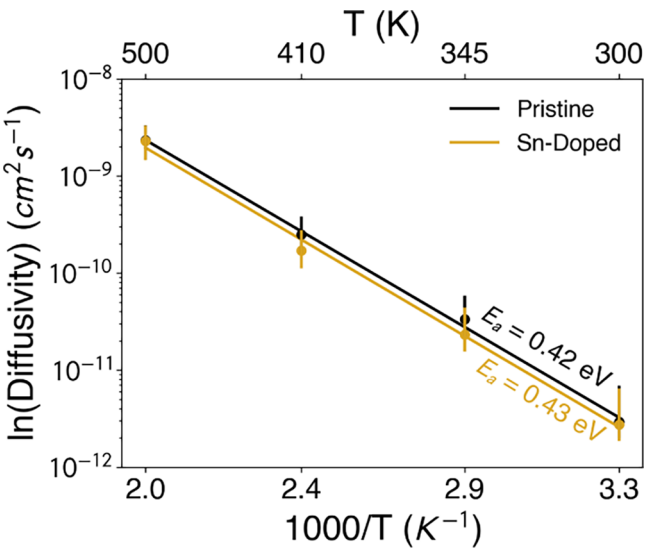


Figure 4. Arrhenius plots of the calculated diffusion coefficients for pristine and 3% Sn-doped γ-$CsPbI_3$.

https://doi.org/10.1021/acs.chemmater.5c00503
Chem. Mater. 2025, 37, 4416−4424

still within the range of energy barriers experimentally found in similar inorganic perovskite systems and show consistent trends with temperature and composition. In DFT-NEB calculations, the migration barriers are computed along a predefined path, which means migrations around Sn are explicitly considered. MD simulations are more representative of experimental conditions, where ion migration occurs via multiple pathways. Given 3% Sn-doping, most of the halide migration still occurs around Pb sites, leading to an average migration barrier that remains similar to the pristine system. We note that, even though Sn-doping can improve efficiencies by reducing the band gap, the similar iodide migration barriers for the pristine and Sn-doped material imply that small amounts of Sn-doping would not directly resolve the long-term stability issue of ion migration-related degradation. Direct comparison with experimental D_I values can be difficult, as they are not straightforward to measure for complex perovskites. Indeed, experimental D_I values for the perovskite $MAPbI_3$ range between 10^{-11} and 10^{-6} cm^2s^{-1} at room temperature[88] which may reflect differences in experimental conditions, thermal history, and phase purity.

Further atomistic insights into the mechanistic features of iodide-ion transport can be gained from visualizing the ion jumps or trajectories from the MD simulations (shown in Figure 5). This illustrates the significant movement of iodide ions in the pristine and Sn-doped structures. The line trajectories also confirm that iodide-ion diffusion occurs via conventional hops between iodide sites along the Pb−I octahedral edges for both systems, in agreement with our DFT simulations. The iodide mobility is not accompanied by any distinct correlated motion of the Pb or Cs ions.

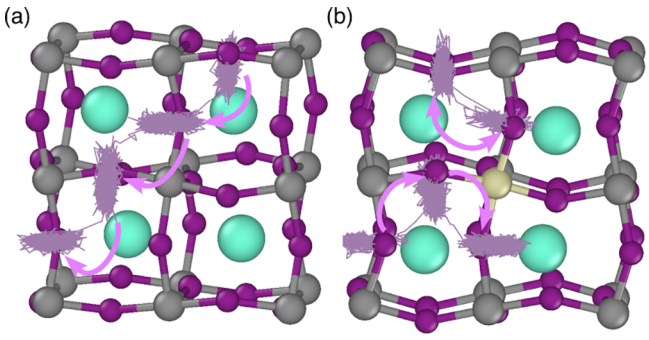


Figure 5. Iodide ion trajectories from the MD simulations (with 1% iodide vacancies) superimposed on the relaxed γ-$CsPbI_3$ lattice to illustrate mechanistic features through (a) the pristine lattice and (b) the Sn-doped lattice.

Additional structural information can be gleaned from the radial distribution function (RDF), which provides insights into the long-range order (or disorder) of perovskite materials. The RDFs for Pb−Pb (shown in Figure 6) reveal a series of sharp peaks for both compositions, with the first coordination shells clearly resolved, in agreement with the observed ordered crystal structure of γ-$CsPbI_3$. In contrast, the RDF for I−I shows a broader, more diffuse structure for separations greater than nearest-neighbor, indicative of greater ion mobility in the iodide sublattice. Additional analysis of the visualized trajectories for all elements, as well as the elemental MSDs, confirms that iodide mobility dominates (Figures S5 and S6). This is more pronounced at higher temperatures, showing lower maxima (Figure 6c). Interestingly, such features are similar to those found in fast-ion-conducting solid electrolytes for fuel cells and lithium batteries, in which the RDFs of the mobile sublattice are commonly more disordered than those of normal crystalline solids.

3. CONCLUSION

Deeper atomic-scale understanding of doping and transport phenomena in inorganic perovskite halides is important for the development of their optoelectronic applications. In this study, we investigated the effect on iodide ion migration of incorporating different cation dopants into orthorhombic γ-$CsPbI_3$.

Three key conclusions emerge. First, the orthorhombic structure, band gap, and ion migration energy from the *ab initio* simulations of γ-$CsPbI_3$ are in good agreement with the available experimental data. The lowest migration activation energy was observed for the iodide ion vacancy pathway between adjacent 8d symmetry sites. Second, by investigating trends in a systematic manner, we find that none of the partial B-site dopant substitutions (including Sn^{2+}, Ba^{2+} and Cu^{2+}) give rise to an appreciable increase in activation energy for iodide migration; certain dopants such as Zn^{2+} lead to lower migration barriers due to local structural relaxations. The

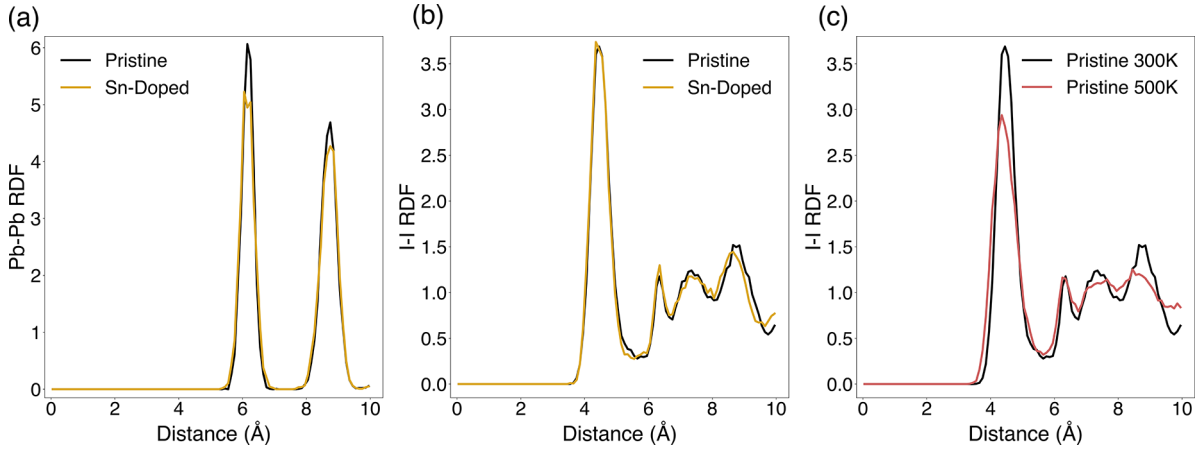


Figure 6. Radial distribution functions (RDFs) of (a) Pb−Pb and (b) I−I in the pristine and Sn-doped compositions at 300 K. (c) I−I (RDFs) for the pristine composition at 300 and 500 K.

https://doi.org/10.1021/acs.chemmater.5c00503
Chem. Mater. 2025, 37, 4416−4424

results, therefore, suggest that these dopants would not significantly suppress iodide ion migration in γ-$CsPbI_3$. Third, a state-of-the-art machine learning interatomic potential model was derived for large-scale MD simulations (~80 ns) of the pristine and Sn-doped materials, which have not been widely employed to examine diffusion mechanisms in inorganic perovskite halides. The results revealed iodide diffusion paths along the Pb−I octahedral edges with no evidence of correlated Pb or Cs motion. Such mechanistic features are difficult to extract from experiments alone. Structural analysis indicates long-range order of the Pb sublattice in agreement with the observed crystalline structure and disorder in the anion sublattice, indicative of high iodide ion mobility. Overall, this study enhances our fundamental understanding of γ-$CsPbI_3$ and provides a framework to guide future doping and ion transport work on these inorganic perovskite solar cell materials to improve their device performance.

4. METHODS

4.1. *Ab Initio* Methods. DFT calculations were performed using the Vienna Ab initio Simulation Package (VASP),[87−90] a plane-wave code with projector-augmented-wave (PAW) pseudopotentials[91,92] which has been extensively used for modeling perovskite solid-state materials. The generalized gradient approximation (GGA) exchange-correlation functional PBEsol[93] was used for all DFT calculations, with a plane-wave cutoff energy of 500 eV and a k-point mesh corresponding to a k-spacing of $0.2/2\pi$ Å^{-1}. Forces were converged to less than 0.01 eV/Å for all structural optimizations. PBEsol was chosen because it provided a balance of computational efficiency and accuracy in replicating structural parameters compared to X-ray diffraction experiments (Table 1).[17] All calculations included spin polarization to ensure that any effects due to unpaired electrons, notably in the defect structures, were captured.[94] Functionals at higher levels of theory were also tested but did not improve the accuracy of predicting structural parameters.

The ion migration pathways were modeled using climbing image nudged elastic band (CI-NEB) calculations[95,96] in VASP. These calculations were performed on 2 × 2 × 2 supercells containing 159 atoms (due to the inclusion of a single I vacancy) which ensured minimal interactions between repeating images. The activation energy of a migration pathway was calculated by subtracting the starting point energy from the energy at the position of highest potential energy, the "saddle point." In each case, the starting and end points were well-converged to avoid inaccuracies in the transition state energy profile. Due to a sufficiently large supercell, these calculations represent migration in the dilute limit without any interactions between migrating ions. This approach has been used successfully in numerous ion migration studies.[33,38,81]

4.2. Machine Learning Methods. The machine-learned interatomic potentials (MLIPs) were trained on ~4,000 structures (Table S1) taken from *ab initio* molecular dynamics (AIMD) simulations and single points derived from the CI-NEB calculations. The energies and forces of each structure were calculated at the same GGA level used for previous DFT calculations. The structures included in the training set covered the pristine system as well as defect configurations containing vacancies and dopants. These MLIPs were trained using MACE, a state-of-the-art equivariant graph neural network model.[72,97] The model has a maximum equivariance order of two, 256 chemical channels, and two layers with a cutoff radius of 5 Å. A single potential model was trained from scratch, which is transferable between the compositions of interest. Evaluations of the model training are shown in Figure S7.

4,3. Diffusion Analysis. The MD simulations were run in LAMMPS[98] on supercells containing 960 atoms with 1% iodide defects at constant volume and constant temperature for ~80 ns. We stress that this simulation timescale is much longer than standard *ab initio* MD simulations, which are typically less than 100 ps. Ionic diffusivities for the iodide ions were extracted from trajectories at four different temperatures arranged linearly on an inverse temperature scale between 300 and 500 K. The MSD plots (Figure S3) and diffusion coefficients were calculated using Kinisi version 1.0.0.[99,100] The diffusion coefficients were calculated from the MSD plots using the following relationship:

$$\mathrm{MSD} = \langle (x(t) - x(0))^2 \rangle = 6Dt \tag{1}$$

and the Arrhenius relationship (eqs. S1, S2) was used to calculate the activation barrier from the diffusion coefficients. Using the form given below, the activation barrier can be found from the slope of the natural log of the diffusion coefficients when plotted vs 1/T.

$$\ln D = -\frac{E_a}{RT} + \ln D_0 \tag{2}$$

■ ASSOCIATED CONTENT

Supporting Information

The Supporting Information is available free of charge at https://pubs.acs.org/doi/10.1021/acs.chemmater.5c00503.

Schottky and Frenkel defect equations, DFT-NEB energy profiles, and additional MLIP information (structures, MSD plots, and training data)(PDF)

■ AUTHOR INFORMATION

Corresponding Author

M. Saiful Islam − *Department of Materials, University of Oxford, Oxford OX1 3PH, U.K.*; orcid.org/0000-0003-3882-0285; Email: saiful.islam@materials.ox.ac.uk

Authors

Allison Nicole Arber − *Department of Materials, University of Oxford, Oxford OX1 3PH, U.K.*

Vikram − *Department of Materials, University of Oxford, Oxford OX1 3PH, U.K.*

Felix C. Mocanu − *Department of Materials, University of Oxford, Oxford OX1 3PH, U.K.*

Complete contact information is available at: https://pubs.acs.org/10.1021/acs.chemmater.5c00503

Author Contributions

The manuscript was written with contributions from all authors. All authors have given their approval to the final version of the manuscript.

Funding

This work was funded by the Engineering and Physical Sciences Research Council (EPSRC), UK (EP/X035859/1).

Notes

The authors declare no competing financial interest.

■ ACKNOWLEDGMENTS

M.S.I. and A.N.A. acknowledge the Department of Materials at the University of Oxford for a DTP studentship. M.S.I. and V. acknowledge the Engineering and Physical Sciences Research Council (EPSRC) Programme Grant (EP/X038777/1) for a postdoctoral fellowship. The authors are grateful to the UK's HEC Materials Chemistry Consortium (EP/X035859/1) for the use of the ARCHER2 high-performance computing facilities and would also like to acknowledge the use of the University of Oxford Advanced Research Computing (ARC) facility in carrying out this work (10.5281/zenodo.22558).

https://doi.org/10.1021/acs.chemmater.5c00503
Chem. Mater. 2025, 37, 4416−4424

REFERENCES

(1) NREL. *Best Research-Cell Efficiency Chart*, 2025. https://www.nrel.gov/pv/cell-efficiency.html. (Accessed 28 February 2025).
(2) Richter, A.; Hermle, M.; Glunz, S. W. Reassessment of the Limiting Efficiency for Crystalline Silicon Solar Cells. *IEEE J. Photovolt.* **2013**, *3* (4), 1184−1191.
(3) Liu, S.; Li, J.; Xiao, W.; Chen, R.; Sun, Z.; Zhang, Y.; Lei, X.; Hu, S.; Kober-Czerny, M.; Wang, J.; et al. Buried interface molecular hybrid for inverted perovskite solar cells. *Nature* **2024**, *632*, 536.
(4) Chen, H.; Liu, C.; Xu, J.; Maxwell, A.; Zhou, W.; Yang, Y.; Zhou, Q.; Bati, A. S. R.; Wan, H.; Wang, Z.; et al. Improved charge extraction in inverted perovskite solar cells with dual-site-binding ligands. *Science* **2024**, *384* (6692), 189−193.
(5) Park, J.; Kim, J.; Yun, H.-S.; Paik, M. J.; Noh, E.; Mun, H. J.; Kim, M. G.; Shin, T. J.; Seok, S. I. Controlled growth of perovskite layers with volatile alkylammonium chlorides. *Nature* **2023**, *616* (7958), 724−730.
(6) Wang, J.; Che, Y.; Duan, Y.; Liu, Z.; Yang, S.; Xu, D.; Fang, Z.; Lei, X.; Li, Y.; Liu, S. 21.15%-Efficiency and Stable γ-$CsPbI_3$ Perovskite Solar Cells Enabled by an Acyloin Ligand. *Adv. Mater.* **2023**, *35* (12), 2210223.
(7) Mali, S. S.; Patil, J. V.; Shao, J.-Y.; Zhong, Y.-W.; Rondiya, S. R.; Dzade, N. Y.; Hong, C. K. Phase-heterojunction all-inorganic perovskite solar cells surpassing 21.5% efficiency. *Nat. Energy* **2023**, *8* (9), 989−1001.
(8) Burschka, J.; Pellet, N.; Moon, S.-J.; Humphry-Baker, R.; Gao, P.; Nazeeruddin, M. K.; Gratzel, M. Sequential deposition as a route to high-performance perovskite-sensitized solar cells. *Nature* **2013**, *499*, 316−319.
(9) Green, M. A.; Ho-Baillie, A.; Snaith, H. J. The emergence of perovskite solar cells. *Nat. Photonics* **2014**, *8* (7), 506−514.
(10) Liu, M.; Johnston, M. B.; Snaith, H. J. Efficient planar heterojunction perovskite solar cells by vapour deposition. *Nature* **2013**, *501*, 395−398.
(11) Beynon, D.; Parvazian, E.; Hooper, K.; McGettrick, J.; Patidar, R.; Dunlop, T.; Wei, Z.; Davies, P.; Garcia-Rodriguez, R.; Carnie, M.; et al. All-Printed Roll-to-Roll Perovskite Photovoltaics Enabled by Solution-Processed Carbon Electrode. *Adv. Mater.* **2023**, *35* (16), 2208561.
(12) Moot, T.; Werner, J.; Eperon, G. E.; Zhu, K.; Berry, J. J.; McGehee, M. D.; Luther, J. M. Choose Your Own Adventure: Fabrication of Monolithic All-Perovskite Tandem Photovoltaics. *Adv. Mater.* **2020**, *32* (50), No. e2003312.
(13) Sutton, R. J.; Eperon, G. E.; Miranda, L.; Parrott, E. S.; Kamino, B. A.; Patel, J. B.; Hörantner, M. T.; Johnston, M. B.; Haghighirad, A. A.; Moore, D. T.; et al. Bandgap-Tunable Cesium Lead Halide Perovskites with High Thermal Stability for Efficient Solar Cells. *Adv. Energy Mater.* **2016**, *6* (8), 1502458.
(14) Liang, J.; Wang, C.; Wang, Y.; Xu, Z.; Lu, Z.; Ma, Y.; Zhu, H.; Hu, Y.; Xiao, C.; Yi, X.; et al. All-Inorganic Perovskite Solar Cells. *J. Am. Chem. Soc.* **2016**, *138* (49), 15829−15832.
(15) Duan, J.; Xu, H.; Sha, W. E. I.; Zhao, Y.; Wang, Y.; Yang, X.; Tang, Q. Inorganic perovskite solar cells: An emerging member of the photovoltaic community. *J. Mater. Chem. A* **2019**, *7* (37), 21036−21068.
(16) Zhou, W.; Zhao, Y.; Zhou, X.; Fu, R.; Li, Q.; Zhao, Y.; Liu, K.; Yu, D.; Zhao, Q. Light-Independent Ionic Transport in Inorganic Perovskite and Ultrastable Cs-Based Perovskite Solar Cells. *J. Phys. Chem. Lett.* **2017**, *8* (17), 4122−4128.
(17) Sutton, R. J.; Filip, M. R.; Haghighirad, A. A.; Sakai, N.; Wenger, B.; Giustino, F.; Snaith, H. J. Cubic or Orthorhombic? Revealing the Crystal Structure of Metastable Black-Phase $CsPbI_3$ by Theory and Experiment. *ACS Energy Lett.* **2018**, *3* (8), 1787−1794.
(18) Eperon, G. E.; Paternò, G. M.; Sutton, R. J.; Zampetti, A.; Haghighirad, A. A.; Cacialli, F.; Snaith, H. J. Inorganic caesium lead iodide perovskite solar cells. *J. Mater. Chem. A* **2015**, *3* (39), 19688−19695.
(19) Bush, K. A.; Palmstrom, A. F.; Yu, Z. J.; Boccard, M.; Cheacharoen, R.; Mailoa, J. P.; McMeekin, D. P.; Hoye, R. L. Z.; Bailie, C. D.; Leijtens, T.; et al. 23.6%-efficient monolithic perovskite/silicon tandem solar cells with improved stability. *Nat. Energy* **2017**, *2* (4), 17009.
(20) Eperon, G. E.; Leijtens, T.; Bush, K. A.; Prasanna, R.; Green, T.; Wang, J. T.-W.; McMeekin, D. P.; Volonakis, G.; Milot, R. L.; May, R.; et al. Perovskite-perovskite tandem photovoltaics with optimized band gaps. *Science* **2016**, *354* (6314), 861−865.
(21) Li, Y.-F.; Feng, J.; Sun, H.-B. Perovskite quantum dots for light-emitting devices. *Nanoscale* **2019**, *11* (41), 19119−19139.
(22) Chiba, T.; Kido, J. Lead halide perovskite quantum dots for light-emitting devices. *J. Mater. Chem. C* **2018**, *6* (44), 11868−11877.
(23) Wang, R.; Shang, C.; Zhao, Q.; Huang, Q.; Liu, C.; Xu, W.; Liu, R.; Zhang, W.; Ding, J. In Situ Generation of Long-Term Stable α-$CsPbI_3$ Nanocrystals in the Cs_4PbI_6 Matrix via Ion Migration. *ACS Appl. Nano Mater.* **2024**, *7* (7), 7632−7641.
(24) Guo, J.; Lu, M.; Zhang, X.; Sun, S.; Han, C.; Zhang, Y.; Yang, X.; Kershaw, S. V.; Zheng, W.; Rogach, A. L. Highly Stable and Efficient Light-Emitting Diodes Based on Orthorhombic gamma-$CsPbI_3$ Nanocrystals. *ACS Nano* **2023**, *17* (10), 9290−9301.
(25) Miao, Y.; Liu, X.; Chen, Y.; Zhang, T.; Wang, T.; Zhao, Y. Deep-Red Perovskite Light-Emitting Diodes Based on One-Step-Formed gamma-$CsPbI_3$ Cuboid Crystallites. *Adv. Mater.* **2021**, *33* (51), No. e2105699.
(26) Lim, S.; Han, S.; Kim, D.; Min, J.; Choi, J.; Park, T. Key Factors Affecting the Stability of $CsPbI_3$ Perovskite Quantum Dot Solar Cells: A Comprehensive Review. *Adv. Mater.* **2023**, *35* (4), No. e2203430.
(27) Siekmann, J.; Ravishankar, S.; Kirchartz, T. Apparent Defect Densities in Halide Perovskite Thin Films and Single Crystals. *ACS Energy Lett.* **2021**, *6* (9), 3244−3251.
(28) Ni, Z.; Bao, C.; Liu, Y.; Jiang, Q.; Wu, W.-Q.; Chen, S.; Dai, X.; Chen, B.; Hartweg, B.; Yu, Z.; et al. Resolving spatial and energetic distributions of trap states in metal halide perovskite solar cells. *Science* **2020**, *367* (6484), 1352−1358.
(29) Mizusaki, J.; Arai, K.; Fueki, K. Ionic conduction of the perovskite-type halides. *Solid State Ionics* **1983**, *11* (3), 203−211.
(30) Narayan, R. L.; Sarma, M. V. S.; Suryanarayana, S. V. Ionic conductivity of $CsPbCl_3$ and $CsPbBr_3$. *J. Mater. Sci. Lett.* **1987**, *6* (1), 93−94.
(31) Kuku, T. A. Ionic transport and galvanic cell discharge characteristics of $CuPbI_3$ thin films. *Thin Solid Films* **1998**, *325*, 246−220.
(32) Senocrate, A.; Moudrakovski, I.; Kim, G. Y.; Yang, T.-Y.; Gregori, G.; Grätzel, M.; Maier, J. The Nature of Ion Conduction in Methylammonium Lead Iodide: A Multimethod Approach. *Angew. Chem. Int. Ed.* **2017**, *56* (27), 7755−7759.
(33) Eames, C.; Frost, J. M.; Barnes, P. R.; O'Regan, B. C.; Walsh, A.; Islam, M. S. Ionic transport in hybrid lead iodide perovskite solar cells. *Nat. Commun.* **2015**, *6*, 7497.
(34) Richardson, G.; O'Kane, S. E. J.; Niemann, R. G.; Peltola, T. A.; Foster, J. M.; Cameron, P. J.; Walker, A. B. Can slow-moving ions explain hysteresis in the current−voltage curves of perovskite solar cells? *Energy Environ. Sci.* **2016**, *9* (4), 1476−1485.
(35) Van Reenen, S.; Kemerink, M.; Snaith, H. J. Modeling Anomalous Hysteresis in Perovskite Solar Cells. *J. Phys. Chem. Lett.* **2015**, *6* (19), 3808−3814.
(36) Zhao, Y.; Zhou, W.; Ma, W.; Meng, S.; Li, H.; Wei, J.; Fu, R.; Liu, K.; Yu, D.; Zhao, Q. Correlations between Immobilizing Ions and Suppressing Hysteresis in Perovskite Solar Cells. *ACS Energy Lett.* **2016**, *1* (1), 266−272.
(37) Meloni, S.; Moehl, T.; Tress, W.; Franckevičius, M.; Saliba, M.; Lee, Y. H.; Gao, P.; Nazeeruddin, M. K.; Zakeeruddin, S. M.; Rothlisberger, U.; et al. Ionic polarization-induced current−voltage hysteresis in $CH_3NH_3PbX_3$ perovskite solar cells. *Nat. Commun.* **2016**, *7* (1), 10334.
(38) Ferdani, D. W.; Pering, S. R.; Ghosh, D.; Kubiak, P.; Walker, A. B.; Lewis, S. E.; Johnson, A. L.; Baker, P. J.; Islam, M. S.; Cameron, P. J. Partial cation substitution reduces iodide ion transport in lead iodide perovskite solar cells. *Energy Environ. Sci.* **2019**, *12* (7), 2264−2272.

https://doi.org/10.1021/acs.chemmater.5c00503
Chem. Mater. 2025, 37, 4416−4424

(39) Hu, Y.; Bai, F.; Liu, X.; Ji, Q.; Miao, X.; Qiu, T.; Zhang, S. Bismuth Incorporation Stabilized α-$CsPbI_3$ for Fully Inorganic Perovskite Solar Cells. *ACS Energy Lett.* **2017**, *2* (10), 2219−2227.
(40) Sa, R.; Luo, B.; Ma, Z.; Liang, L.; Liu, D. Revealing the influence of B-site doping on the physical properties of $CsPbI_3$: A DFT investigation. *J. Solid State Chem.* **2022**, *309*, 122956.
(41) Steele, J. A.; Prakasam, V.; Huang, H.; Solano, E.; Chernyshov, D.; Hofkens, J.; Roeffaers, M. B. J. Trojans That Flip the Black Phase: Impurity-Driven Stabilization and Spontaneous Strain Suppression in γ-$CsPbI_3$ Perovskite. *J. Am. Chem. Soc.* **2021**, *143* (28), 10500−10508.
(42) Pering, S. R.; Deng, W.; Troughton, J. R.; Kubiak, P. S.; Ghosh, D.; Niemann, R. G.; Brivio, F.; Jeffrey, F. E.; Walker, A. B.; Islam, M. S.; et al. Azetidinium lead iodide for perovskite solar cells. *J. Mater. Chem. A* **2017**, *5* (39), 20658−20665.
(43) De Marco, N.; Zhou, H.; Chen, Q.; Sun, P.; Liu, Z.; Meng, L.; Yao, E.-P.; Liu, Y.; Schiffer, A.; Yang, Y. Guanidinium: A Route to Enhanced Carrier Lifetime and Open-Circuit Voltage in Hybrid Perovskite Solar Cells. *Nano Lett.* **2016**, *16* (2), 1009−1016.
(44) Cao, J.; Tao, S. X.; Bobbert, P. A.; Wong, C.-P.; Zhao, N. Interstitial Occupancy by Extrinsic Alkali Cations in Perovskites and Its Impact on Ion Migration. *Adv. Mater.* **2018**, *30* (26), 1707350.
(45) Zhu, H.; Hao, C.; Li, X.; Qi, Y.; Zhu, X.; Miao, Y.; Liu, R.; Ding, J. Long-Term Stability in α-$CsPbI_3$ Quantum Dots via a Nonvacuum Ag^+ Doping Strategy. *J. Phys. Chem. C* **2023**, *127* (37), 18727−18735.
(46) Zhang, M.; Xiang, G.; Wu, Y.; Liu, J.; Leng, J.; Cheng, C.; Ma, H. Revealing the influence of doping elements (Ge, Sn, Ca, and Sr) on the properties of α-$CsPbI_3$: A DFT investigation. *Opt. Express* **2023**, *31* (17), 28624.
(47) Roy, B.; Mahato, S.; Bose, S.; Ghorai, A.; Srivastava, S. K.; Das, N. C.; Ray, S. K. Cu-Doping Induced Phase Transformation in $CsPbI_3$ Nanocrystals with Enhanced Structural Stability and Photoluminescence Quantum Yield. *Chem. Mater.* **2023**, *35* (4), 1601−1609.
(48) Torres, I. S.; Da Silva, J. L. F.; Lima, M. P. The Role of M^{3+} Substitutional Doping (M = In, Sb, Bi) in the Passivation of the α-$CsPbI_3$ (100) Surface. *J. Phys. Chem. C* **2023**, *127* (4), 1713−1721.
(49) Fang, Z.; Shang, M. H.; Hou, X. M.; Zheng, Y. P.; Du, Z. T.; Yang, Z. B.; Chou, K. C.; Yang, W. Y.; Wang, Z. L.; Yang, Y. Bandgap alignment of alpha-$CsPbI_3$ perovskites with synergistically enhanced stability and optical performance via B-site minor doping. *Nano Energy* **2019**, *61*, 389−396.
(50) Bera, S.; Ghosh, D.; Dutta, A.; Bhattacharyya, S.; Chakraborty, S.; Pradhan, N. Limiting Heterovalent B-Site Doping in $CsPbI_3$ Nanocrystals: Phase and Optical Stability. *ACS Energy Lett.* **2019**, *4* (6), 1364−1369.
(51) Chen, Y.; Jing, H.; Ling, F.; Kang, W.; Zhou, T.; Liu, X.; Zeng, W.; Zhang, Y.; Qi, L.; Fang, L.; et al. Tuning the electronic structures of all-inorganic lead halide perovskite $CsPbI_3$ via heterovalent doping: A first-principles investigation. *Chem. Phys. Lett.* **2019**, *722*, 90−95.
(52) Lu, M.; Zhang, X.; Zhang, Y.; Guo, J.; Shen, X.; Yu, W. W.; Rogach, A. L. Simultaneous Strontium Doping and Chlorine Surface Passivation Improve Luminescence Intensity and Stability of $CsPbI_3$ Nanocrystals Enabling Efficient Light-Emitting Devices. *Adv. Mater.* **2018**, *30* (50), 1804691.
(53) Lu, M.; Zhang, X.; Bai, X.; Wu, H.; Shen, X.; Zhang, Y.; Zhang, W.; Zheng, W.; Song, H.; Yu, W. W.; et al. Spontaneous Silver Doping and Surface Passivation of $CsPbI_3$ Perovskite Active Layer Enable Light-Emitting Devices with an External Quantum Efficiency of 11.2%. *ACS Energy Lett.* **2018**, *3* (7), 1571−1577.
(54) Xiang, S.; Li, W.; Wei, Y.; Liu, J.; Liu, H.; Zhu, L.; Chen, H. The synergistic effect of non-stoichiometry and Sb-doping on air-stable alpha-$CsPbI_3$ for efficient carbon-based perovskite solar cells. *Nanoscale* **2018**, *10* (21), 9996−10004.
(55) Euvrard, J.; Yan, Y.; Mitzi, D. B. Electrical doping in halide perovskites. *Nat. Rev. Mater.* **2021**, *6* (6), 531−549.
(56) Sidiq, D. H.; Mahato, S.; Haposan, T.; Makowski, M.; Kowal, D.; Witkowski, M. E.; Drozdowski, W.; Arramel; Birowosuto, M. D. Cation Engineering of Cu-Doped $CsPbI_3$: Lead Substitution and Dimensional Reduction for Improved Scintillation Performance. *J. Phys. Chem. C* **2024**, *128* (47), 20324−20332.
(57) Lee, C.; Chae, K.; Ko, Y.; Lee, C.; Kim, T.; Park, S.; Jung, M. Y.; Kim, J.; Yun, Y. J.; Lee, M.; et al. Phase Stability Improvement of a gamma-$CsPbI_3$ Perovskite Solar Cell Utilizing a Barium Bis-(trifluoromethanesulfonimide) Solution. *ACS Appl. Mater. Interfaces* **2023**, *15* (44), 51050−51058.
(58) Pansa-Ngat, P.; Singh, K.; Patel, B.; Seriwattanachai, C.; Kanjanaboos, P.; Voznyy, O. Stereoelectronic Effect from B-Site Dopants Stabilizes Black Phase of $CsPbI_3$. *Chem. Mater.* **2023**, *35* (1), 271−279.
(59) Evarestov, R. A.; Senocrate, A.; Kotomin, E. A.; Maier, J. First-principles calculations of iodine-related point defects in $CsPbI_3$. *Phys. Chem. Chem. Phys.* **2019**, *21* (15), 7841−7846.
(60) Walsh, A.; Stranks, S. D. Taking Control of Ion Transport in Halide Perovskite Solar Cells. *ACS Energy Lett.* **2018**, *3* (8), 1983−1990.
(61) Seidu, A.; Dvorak, M.; Rinke, P.; Li, J. Atomic and electronic structure of cesium lead triiodide surfaces. *J. Chem. Phys.* **2021**, *154* (7), 074712.
(62) Kaczkowski, J.; Płowas-Korus, I. The Vibrational and Thermodynamic Properties of $CsPbI_3$ Polymorphs: An Improved Description Based on the SCAN meta-GGA Functional. *J. Phys. Chem. Lett.* **2021**, *12* (28), 6613−6621.
(63) Fadla, M. A.; Bentria, B.; Dahame, T.; Benghia, A. First-principles investigation on the stability and material properties of all-inorganic cesium lead iodide perovskites $CsPbI_3$ polymorphs. *Phys. B* **2020**, *585*, 412118.
(64) Huang, Y.; Yin, W.-J.; He, Y. Intrinsic Point Defects in Inorganic Cesium Lead Iodide Perovskite $CsPbI_3$. *J. Phys. Chem. C* **2018**, *122* (2), 1345−1350.
(65) Marronnier, A.; Roma, G.; Boyer-Richard, S.; Pedesseau, L.; Jancu, J.-M.; Bonnassieux, Y.; Katan, C.; Stoumpos, C. C.; Kanatzidis, M. G.; Even, J. Anharmonicity and Disorder in the Black Phases of Cesium Lead Iodide Used for Stable Inorganic Perovskite Solar Cells. *ACS Nano* **2018**, *12* (4), 3477−3486.
(66) Gonzalez, J. E.; Danelon, J. G.; Da Silva, J. L. F.; Lima, M. P. Elucidating Black alpha-$CsPbI_3$ Perovskite Stabilization via PPD Bication-Conjugated Molecule Surface Passivation: Ab Initio Simulations. *ACS Appl. Mater. Interfaces* **2024**, *16* (30), 39251−39265.
(67) Han, M.; Peng, C.; Song, R.; Ke, F.; Nashed, Y. S. G.; Mao, W. L.; Jia, C.; Lin, Y. Machine learning-empowered study of metastable γ-$CsPbI_3$ under pressure and strain. *J. Mater. Chem. A* **2024**, *12* (18), 11082−11089.
(68) Kweon, K. E.; Varley, J.; Ogitsu, T.; Wan, L. F.; Shelby, M.; Song, Z.; Ellingson, R. J.; Yan, Y.; Lee, J. R. I. Influence of External Conditions on the Black-to-Yellow Phase Transition of $CsPbI_3$ Based on First-Principles Calculations: Pressure and Moisture. *Chem. Mater.* **2023**, *35* (6), 2321−2329.
(69) Ke, F.; Wang, C.; Jia, C.; Wolf, N. R.; Yan, J.; Niu, S.; Devereaux, T. P.; Karunadasa, H. I.; Mao, W. L.; Lin, Y. Preserving a robust $CsPbI_3$ perovskite phase via pressure-directed octahedral tilt. *Nat. Commun.* **2021**, *12* (1), 461.
(70) Stoumpos, C. C.; Kanatzidis, M. G. The Renaissance of Halide Perovskites and Their Evolution as Emerging Semiconductors. *Acc. Chem. Res.* **2015**, *48* (10), 2791−2802.
(71) Zhang, J.; Shang, M.-H.; Wang, P.; Huang, X.; Xu, J.; Hu, Z.; Zhu, Y.; Han, L. n-Type Doping and Energy States Tuning in $CH_3NH_3Pb_{1-x}Sb_{2x/3}I_3$ Perovskite Solar Cells. *ACS Energy Lett.* **2016**, *1* (3), 535−541.
(72) Batatia, I.; Batzner, S.; Kovács, D. P.; Musaelian, A.; Simm, G. N. C.; Drautz, R.; Ortner, C.; Kozinsky, B.; Csányi, G. The design space of E(3)-equivariant atom-centred interatomic potentials. *Nat. Mach. Intell.* **2025**, *7* (1), 56−67.
(73) Walsh, A.; Scanlon, D. O.; Chen, S.; Gong, X. G.; Wei, S. H. Self-Regulation Mechanism for Charged Point Defects in Hybrid Halide Perovskites. *Angew. Chem. Int. Ed.* **2015**, *54* (6), 1791−1794.

https://doi.org/10.1021/acs.chemmater.5c00503
Chem. Mater. 2025, 37, 4416−4424

(74) Islam, M. S. Ionic transport in ABO_3 perovskite oxides: A computer modelling tour. *J. Mater. Chem.* **2000**, *10* (4), 1027−1038.
(75) Yashima, M.; Nomura, K.; Kageyama, H.; Miyazaki, Y.; Chitose, N.; Adachi, K. Conduction path and disorder in the fast oxide-ion conductor $(La_{0.8}Sr_{0.2})(Ga_{0.8}Mg_{0.15}Co_{0.05})O_{2.8}$. *Chem. Phys. Lett.* **2003**, *380* (3−4), 391−396.
(76) Kuku, T. A. Structure and ionic conductivity of $CuCdCl_3$. *Solid State Ionics* **1987**, *25* (2), 105−108.
(77) Narayan, R. L.; Suryanarayana, S. V. Transport properties of the perovskite-type halides. *Mater. Lett.* **1991**, *11* (8), 305−308.
(78) Nur'aini, A.; Lee, S.; Oh, I. Ion Migration in Metal Halide Perovskites. *J. Electrochem. Sci. Technol.* **2022**, *13* (1), 71−77.
(79) Balestra, S. R. G.; Vicent-Luna, J. M.; Calero, S.; Tao, S.; Anta, J. A. Efficient modelling of ion structure and dynamics in inorganic metal halide perovskites. *J. Mater. Chem. A* **2020**, *8* (23), 11824−11836.
(80) Aristidou, N.; Eames, C.; Sanchez-Molina, I.; Bu, X.; Kosco, J.; Islam, M. S.; Haque, S. A. Fast oxygen diffusion and iodide defects mediate oxygen-induced degradation of perovskite solar cells. *Nat. Commun.* **2017**, *8*, 15218.
(81) Senocrate, A.; Spanopoulos, I.; Zibouche, N.; Maier, J.; Islam, M. S.; Kanatzidis, M. G. Tuning Ionic and Electronic Conductivities in the "Hollow" Perovskite $MAPbI_3$. *Chem. Mater.* **2021**, *33* (2), 719−726.
(82) Dey, K.; Ghosh, D.; Pilot, M.; Pering, S. R.; Roose, B.; Deswal, P.; Senanayak, S. P.; Cameron, P. J.; Islam, M. S.; Stranks, S. D. Substitution of lead with tin suppresses ionic transport in halide perovskite optoelectronics. *Energy Environ. Sci.* **2024**, *17* (2), 760−769.
(83) Godt, J.; Scheidig, F.; Grosse-Siestrup, C.; Esche, V.; Brandenburg, P.; Reich, A.; Groneberg, D. A. The toxicity of cadmium and resulting hazards for human health. *J. Occup. Med. Toxicol.* **2006**, *1* (1), 22.
(84) Hu, S.; Thiesbrummel, J.; Pascual, J.; Stolterfoht, M.; Wakamiya, A.; Snaith, H. J. Narrow Bandgap Metal Halide Perovskites for All-Perovskite Tandem Photovoltaics. *Chem. Rev.* **2024**, *124* (7), 4079−4123.
(85) Yang, S.; Wu, M.; Lei, X.; Wang, J.; Han, Y.; He, X.; Liu, S.; Liu, Z. Ultra-High 1.27 V VOC of Pure $CsPbI_3$ Perovskite Solar Cells with an Efficiency of 21.8%. *ACS Energy Lett.* **2024**, *9* (10), 4817−4826.
(86) Reichert, S.; Flemming, J.; An, Q.; Vaynzof, Y.; Pietschmann, J.-F.; Deibel, C. Ionic-Defect Distribution Revealed by Improved Evaluation of Deep-Level Transient Spectroscopy on Perovskite Solar Cells. *Phys. Rev. Appl.* **2020**, *13* (3), 034018.
(87) Horoz, S.; Simsek, S.; Palaz, S.; Mamedov, A. M. Electronic and Optical Properties of Rare Earth Oxides: Ab Initio Calculation. *World J. Condens. Matter. Phys.* **2015**, *05* (2), 78−85.
(88) Kresse, G.; Furthmüller, J. Efficient iterative schemes for ab initio total-energy calculations using a plane-wave basis set. *Phys. Rev. B* **1996**, *54* (16), 11169−11186.
(89) Kresse, G.; Hafner, J. Ab initio molecular dynamics for liquid metals. *Phys. Rev. B* **1993**, *47* (1), 558−561.
(90) Seriy, S. Modern Ab-Initio Calculations on Modified Tomas-Fermi−Dirac Theory. *Open J. Modell. Simul.* **2015**, *03* (3), 96−103.
(91) Blöchl, P. E. Projector augmented-wave method. *Phys. Rev. B* **1994**, *50* (24), 17953−17979.
(92) Kresse, G.; Joubert, D. From ultrasoft pseudopotentials to the projector augmented-wave method. *Phys. Rev. B* **1999**, *59* (3), 1758−1775.
(93) Perdew, J. P.; Ruzsinszky, A.; Csonka, G. I.; Vydrov, O. A.; Scuseria, G. E.; Constantin, L. A.; Zhou, X.; Burke, K. Restoring the Density-Gradient Expansion for Exchange in Solids and Surfaces. *Phys. Rev. Lett.* **2008**, *100*, 136406.
(94) Woo, Y. W.; Jung, Y.-K.; Kim, G. Y.; Kim, S.; Walsh, A. Factors influencing halide vacancy transport in perovskite solar cells. *Discover Mater.* **2022**, *2* (1), 8.
(95) Henkelman, G.; Jónsson, H. Improved tangent estimate in the nudged elastic band method for finding minimum energy paths and saddle points. *J. Chem. Phys.* **2000**, *113* (22), 9978−9985.
(96) Henkelman, G.; Uberuaga, B. P.; Jónsson, H. A climbing image nudged elastic band method for finding saddle points and minimum energy paths. *J. Chem. Phys.* **2000**, *113* (22), 9901−9904.
(97) Batatia, I.; Kovacs, D. P.; Gregor, S. N. C.; Ortner, C.; Csanyi, G. M. Higher Order Equivariant Message Passing Neural Networks for Fast and Accurate Force Fields. *arXiv*. **2023** (v2).
(98) Thompson, A. P.; Aktulga, H. M.; Berger, R.; Bolintineanu, D. S.; Brown, W. M.; Crozier, P. S.; in't Veld, P. J.; Kohlmeyer, A.; Moore, S. G.; Nguyen, T. D.; et al. LAMMPS - a flexible simulation tool for particle-based materials modeling at the atomic, meso, and continuum scales. *Comput. Phys. Commun.* **2022**, *271*, 108171.
(99) McCluskey, A. R.; Squires, A. G.; Dunn, J.; Coles, S. W.; Morgan, B. J. kinisi: Bayesian analysis of mass transport from molecular dynamics simulations. *J. Open Source Softw.* **2024**, *9* (94), 5984.
(100) McCluskey, A. R.; Coles, S. W.; Morgan, B. J. Accurate Estimation of Diffusion Coefficients and their Uncertainties from Computer Simulation. *J. Chem. Theory Comput.* **2025**, *21* (1), 79−87.

https://doi.org/10.1021/acs.chemmater.5c00503
Chem. Mater. 2025, 37, 4416−4424